

Article

Self-Assembled Fullerene Crystals as Excellent Aromatic Vapor Sensors

Natsumi Furuuchi ¹, Rekha Goswami Shrestha ² , Yuji Yamashita ¹, Tetsuji Hirao ¹, Katsuhiko Ariga ^{2,3}  and Lok Kumar Shrestha ^{2,*} 

¹ Graduate School of Pharmaceutical Science, Chiba Institute of Science, 15-8 Shiomi-cho, Choshi-shi, Chiba 288-0025, Japan; pm16p04@cis.ac.jp (N.F.); yyamashita@cis.ac.jp (Y.Y.); thirao@cis.ac.jp (T.H.)

² International Center for Materials Nanoarchitectonics (WPI-MANA), National Institute for Materials Science (NIMS), 1-1 Namiki, Ibaraki Tsukuba 305-0044, Japan; rekhashrestha3@hotmail.com (R.G.S.); ARIGA.Katsuhiko@nims.go.jp (K.A.)

³ Graduate School of Frontier Science, The University of Tokyo, Kashiwa, Chiba 277-0827, Japan

* Correspondence: SHRESTHA.Lokkumar@nims.go.jp; Tel.: +81-29-860-4809

Received: 10 December 2018; Accepted: 8 January 2019; Published: 11 January 2019



Abstract: Here we report the aromatic vapor sensing performance of bitter melon shaped nanoporous fullerene C₆₀ crystals that are self-assembled at a liquid-liquid interface between isopropyl alcohol and C₆₀ solution in dodecylbenzene at 25 °C. Average length and center diameter of the crystals were ca. 10 μm and ~2 μm, respectively. Powder X-ray diffraction pattern (pXRD) confirmed a face-centered cubic (*fcc*) structure with cell dimension ca. $a = 1.4272$ nm, and $V = 2.907$ nm³, which is similar to that of the pristine fullerene C₆₀. Transmission electron microscopy (TEM) confirmed the presence of a nanoporous structure. Quartz crystal microbalance (QCM) results showed that the bitter melon shaped nanoporous C₆₀ performs as an excellent sensing system, particularly for aromatic vapors, due to their easy diffusion through the porous architecture and strong π - π interactions with the *sp*²-carbon.

Keywords: fullerene crystals; self-assembly; liquid-liquid interface; aromatic vapors; quartz crystal microbalance; sensing

1. Introduction

Fullerene (C₆₀) is a truncated icosahedron (I_h) consisting of purely carbon atoms positioned at the junction of a series of hexagons (20) and pentagons (12) arranged in a cage lattice (diameter ~0.8 nm) and defined by alternating single and double bonds. Due to its excellent redox, optical and optoelectronic properties [1–5], it is an extensively studied nanomaterial in the family of carbon allotropes. After the discovery of fullerene (C₆₀) in 1985 substantial advances in fullerene chemistry lead to a number of interesting developments such as carbon nanotubes (CNTs) and graphene [6,7]. Due to energetically unstable double bonds within the pentagon rings, fullerenes display electron accepting properties, i.e., fullerenes are highly electron deficient molecules. Additionally, reactivity of the fullerene molecules increases due to the curvature induced by the cage structure that increases the energy associated with the double bonds. It has been shown that fullerene C₆₀ molecules polymerize at high temperature and pressure and also under exposure to ultraviolet (UV) light [8,9].

Production of functional materials from molecular units requires essential contributions from nanotechnology such as self-assembly/or self-organization, supramolecular assembly, nanomaterials fabrication or nanobiotechnology [10–15]. Supramolecular assemblies of fullerene (C₆₀) in the bulk phase or at solid substrate using π -stacking interactions enables the production of shape-controlled nano- micro size objects. Well-ordered one-dimensional (1D), two-dimensional (2D) or three-dimensional (3D) forms of

fullerene promote the electronic and optical properties, which are essential to design advanced devices or functional systems [16–18]. Therefore, studies of the self-assembly of fullerenes in well-defined shape continue to grow [19,20].

Several methods such as slow evaporation, vapor deposition, precipitation or re-precipitation and template methods have been proposed for designing the shape-controlled crystalline fullerene objects [21–26]. It should be noted that a particular method generally produces a specific morphology. For example, slow evaporation of fullerene solutions in good solvents yields 1D nanostructures. In this method, the aspect ratio of 1D nanostructure can be controlled by the rate of evaporation, temperature and concentration of fullerene. The second method includes vapor deposition on solid substrate, which commonly gives 2D sheet or thin films. Soft- or hard templating methods have also been proposed to design crystalline fullerene materials. Precipitation or re-precipitation methods generally produce 1D rods or tubes and sometimes aggregates with unique fullerene crystal shapes. However, the liquid-liquid interfacial precipitation (LLIP) method developed by Miyazawa and coworkers [27] produces low to higher dimensional fullerene nanostructures. Fullerene crystals of a wide variety of morphologies have been produced using this method. In the LLIP method, alcohol (the antisolvent of fullerene) is slowly added into a fullerene solution in a good solvent (generally aromatic solvents in which fullerenes are soluble) to form a clear liquid-liquid interface [28–31]. With time alcohol molecules diffuse down towards the good solvent side (alcohols mix well with good solvents) causing an unsaturation at the liquid-liquid interface and as a result crystal nuclei are formed, which will grow further upon diffusion of fullerene from the bulk phase to the interface. The crystal formation mechanism is therefore driven by supersaturation related to the low solubility of fullerene in alcohol, which indicates the importance of the solubility difference of fullerene in the antisolvent and solvent. Needle-like crystals grown in arbitrary directions were observed through the LLIP process at the interface of C_{60} solution in toluene (saturated) and isopropyl alcohol (IPA). Under certain condition, the diameter of the 1D structure was ca. few hundreds of nanometers while lengths were in the hundreds of microns range. Such high aspect ratio 1D nanostructures of fullerene are referred to as fullerene nanowhiskers. Note that contrary to the CNTs, fullerene nanowhiskers do not contain any long-range hollow spaces [32]. Instead, fullerene nanowhiskers are composed of merely fullerene molecules bonded through a combination of Van der Waals interactions and/or chemical bonds (if polymerized). Therefore, they are more bio-friendly and biocompatible. The LLIP method could also be extended to design microporous/mesoporous nanowhiskers or hexagonal nano-/micro-sheets [29,33]. Masuhara et al. [34] have demonstrated fine C_{60} crystals with tunable shape and size by subtle changes in the antisolvent and solvent mixing ratio and temperature. Similarly, Jeong et al. [35] confirmed the multidimensional morphologies of C_{60} microcrystals depending on the type of antisolvent (alcohol type). We have also explored the effect of surfactants on the self-assembly of fullerene at the liquid-liquid interface and found that surfactants, due to their surface-active properties, indeed alter the morphology of the assembled crystals. For instance, in the absence of surfactant 1D C_{60} nanowhiskers (nanorods) and C_{60} nanotubes (diameter 400 nm–2 μ m and length 5–20 μ m) are obtained from a butanol/benzene system. However, when 0.01% diglycerol monolaurate nonionic surfactant is incorporated into the butanol, flower-like microcrystals with average sizes in the range of 10–35 μ m consisting of C_{60} nanotubes are observed [36]. Similarly, C_{60} crystals synthesized at a liquid-liquid interface comprised of IPA and C_{60} solution in ethylbenzene (saturated) exhibited 1D morphology with well-defined faceted structures with average length and diameters of ca. 4.8 μ m and 747 nm, respectively. X-ray diffraction patterns confirmed a hexagonal-close packed (*hcp*) structure with cell dimensions ca. $a = 2.394$ nm, and $c = 1.388$ nm. However, interestingly the 1D rod morphology of C_{60} crystals was transformed into “Konpeito candy” type crystals (average diameter ca. 1.2 μ m) when the C_{60} crystals were grown in the presence of diglycerol monolaurate surfactant [37]. Not only the morphology was affected as the surfactant also caused a structural transformation from *hcp* to the face-centered cubic (*fcc*) crystal phase with cell dimensions of ca. $a = 1.4309$ nm.

Using the LLIP method we succeeded at fabricating complex 3D network structures or hierarchical superstructures [38,39]. For example, cube-shape C_{60} -fullerene-Ag(I) organometallic heteronanostructures undergo an irreversible structural rearrangement upon exposure to low molecular weight alcohols resulting in the formation of cube-shaped arrays of fullerene nanorods which mimic the original cubic crystal morphology and internal structure [40]. Another interesting example includes 3D cubic-shape assembly of fullerene C_{70} molecules, which could be formed using ultrasonic-agitated liquid-liquid interfacial precipitation between a mesitylene solution of C_{70} and *tert*-butyl alcohol (TBA). Upon exposure to IPA at ambient condition, the C_{70} cubic assemblies were converted into a hierarchical structure of needles protruding out of the cube [41]. Interestingly, the needle-like 1D crystals possess nanoporous structures. These hierarchical nanostructures are advantageous due to their high surface areas, synergistic interactions and multiple functionalities, which are not possible to achieve with conventional materials. Self-assembled fullerene or other nanomaterials have attracted much attention as new materials because of their excellent properties and functions, which largely depend on the size, morphology, surface properties and hierarchy [42–45]. Note that insertion of micro- or mesopore structures in the fullerene crystals increases the specific surface area and porosity drastically. Such porous fullerene crystals are essentially required in applications like volatile organic compound (VOC) sensing and electrical double layer supercapacitors. However, despite a huge potential applications in energy storage and sensing, nanoporous (micro/mesoporous) fullerene crystals have not well explored [46,47].

In this contribution, we report the assembly of C_{60} into unique bitter melon shaped nanoporous crystals. This unique C_{60} crystal was produced by a modified liquid-liquid interfacial precipitation (LLIP) method at 25 °C. Due to a well-developed nanoporous structure the bitter melon shape C_{60} crystals showed excellent vapor sensing performance selective towards aromatic vapors favored by easy diffusion through the porous architecture and strong π - π interactions with the sp^2 -carbon. We believe hierarchical micro/mesoporous fullerene-based nanomaterial would be an asset to the sensing technology, particularly to sense aromatic guest molecules.

2. Materials and Methods

2.1. Materials

Pristine fullerene C_{60} (p C_{60}) powder (purity 99.9%) was purchased from MTR Ltd., Cleveland, OH, USA. Isopropyl alcohol (IPA) of purity >99% was purchased from the Wako Chemical Corporation, Tokyo, Japan. Dodecyl benzene purity >99% was a product of Tokyo Chemical Industry, Tokyo, Japan. All these products were used as received.

2.2. Self-Assembly of Fullerene C_{60} at Liquid-Liquid Interface

Fullerene C_{60} crystals were synthesized using a modified liquid-liquid interfacial precipitation (LLIP) method. In a typical crystals synthesis, isopropyl alcohol (IPA: 5 mL) was slowly added into a C_{60} solution in dodecylbenzene (1 mL: 1 mg/mL) so that a clear liquid-liquid interface is formed between the two solutions. The mixture was incubated at 25 °C for about 30 min avoiding any external mechanical disturbances. The mixture was then sonicated for 5 min in a bath sonicator 3510 BRANSON (Gaithersburg, MD, USA) at 100 W followed by vigorous vortex mixing for 1 min. Finally the mixture was incubated at 25 °C for 24 h. The precipitates (self-assembled crystals) were collected by centrifugation and denoted as 'as prepared' sample. The as prepared crystals were washed with excess of IPA (10 mL) and dried in vacuum at 80 °C for further characterizations.

2.3. Characterizations

The prepared self-assembled fullerene nanomaterials (before and IPA after washing) were characterized by powder X-ray diffraction (RINT2000 diffractometer, Rigaku, Tokyo, Japan, with $Cu-K\alpha$ radiation ($\lambda = 0.1541$ nm, scanning electron microscopy (SEM: Model SU-8000, Hitachi Tokyo, Japan)

which was operated at 10 kV), transmission electron microscopy (TEM, Model JEM-2100F operated at 200 kV, JEOL, Tokyo, Japan), Raman scattering spectroscopy (T64000, Jobin-Yvon Edison, Edison, NJ, USA) at a wavelength of 514.5 nm and Fourier transform infrared (FT-IR) spectroscopy (model 4700 instrument, Nicolet, Waltham, MA, USA). For the preparation of SEM samples, a dilute suspensions of fullerene crystals in IPA were drop casted on a clean silicon wafer and dried at 80 °C for 6 h. All the SEM samples were coated with platinum (~2 nm) by sputtering using a Hitachi S-2030 ion coater. TEM samples were prepared by dropping suspensions of fullerene crystal onto standard carbon-coated copper grids. TEM samples were dried at 80 °C in vacuum for 24 h.

2.4. Vapor Sensing by Quartz Crystal Microbalance (QCM)

Quartz crystal microbalance (QCM) is a powerful technique for detection of small changes in mass during thin film deposition, gas adsorption or desorption and structural changes. In the present study, we used a resonance frequency of 9 MHz (AT-cut) and the frequency change of the Au-resonator coated with our material (QCM electrode) was measured during adsorption of vapor phase. Frequency of the QCM electrode in air was stable within ± 2 Hz over more than 10 min. QCM sensor electrode was prepared as follows. Bitter melon shape C₆₀ crystals (0.5 mg) were dispersed in ethanol (1 mL) and vortex shaken for 30 s. Note that dispersion in ethanol did not change the morphology of the prepared crystals. 2 μ L of the resulting suspension was then drop casted onto the QCM electrode (Au resonator). The electrode was dried at 80 °C in vacuum for 12 h. The modified QCM electrode was then set in the instrument and exposed to different solvents vapors (10 mL) at 25 °C in a sealed chamber to prevent the escape of vapors during the adsorption measurements, i.e., the atmosphere is saturated with the solvent vapors. Once the frequency change reached equilibrium, the electrode was exposed to air to desorb the vapor. Repeatability of the QCM electrode was also tested by recording the time dependence of frequency shift (Δf) during alternate exposure and removal of the solvent vapors. VOC sensing performance of the bitter-melon shape nanoporous fullerene crystals was also compared with pristine C₆₀ and as prepared crystal without nanopores before IPA washing. For this purpose, QCM electrodes were prepared following the similar method so that the mass of active materials loaded are essentially the same (1 μ g).

The change in mass m (g cm^{-2}) of the sample deposited on the QCM electrode can be measured by the oscillating frequency of the quartz electrode. The frequency change (Δf) corresponds to amount of sample loaded on the QCM electrode, which can be calculated from the Sauerbrey equation:

$$\Delta f = \left(\frac{2f_0^2}{A\sqrt{\rho_Q\mu_Q}} \Delta m \right) \quad (1)$$

where f_0 (Hz) is the natural frequency of the quartz crystal, Δm is mass change (g), A is area between electrodes (cm^2), ρ_Q is quartz density (2.649 g cm^{-3}) and μ_Q is the shear modulus ($2.947 \times 10^{11} \text{ g cm}^{-1} \text{ s}^2$).

3. Results

The surface morphology of self-assembled fullerene C₆₀ crystals synthesized at 25 °C using the modified liquid-liquid interfacial precipitation (LLIP) method at an interface of isopropyl alcohol (IPA: 5 mL) and C₆₀ solution in dodecylbenzene (1 mL: 1 mg/mL) was studied by scanning electron microscopy (SEM). SEM images of both the samples (as prepared crystals before and after IPA washing) were taken. SEM observations revealed the unique assembly fullerene C₆₀ into bitter melon shaped crystals (Figure 1a–f). The as-prepared crystals before washing appear in aggregated form (Figure S1: see Electronic Supporting Information). Washing with IPA caused segregation of the crystals. High resolution SEM image shows that the individual crystal possesses a rough surface along its entire length. Figure 1g,h shows histograms of length and diameter distributions of randomly selected 100 crystals. Note that the diameter of the crystal is not uniform along the axial length. The diameter in the histogram is referred to the center diameter. a histogram of the length

distribution shows that lengths of crystals are in the range of ~ 6.5 to $13.5 \mu\text{m}$ with majority of crystal exhibiting lengths of $\sim 10 \mu\text{m}$ (Figure 1g). The histogram of center diameters suggests a mean diameter of $2 \mu\text{m}$ (Figure 1h). SEM images also show that some of the crystals are interconnected into different shapes such as T-shapes, Y-shapes, and star-shapes, indicating the anisotropic growth of the crystals (Figure S2).

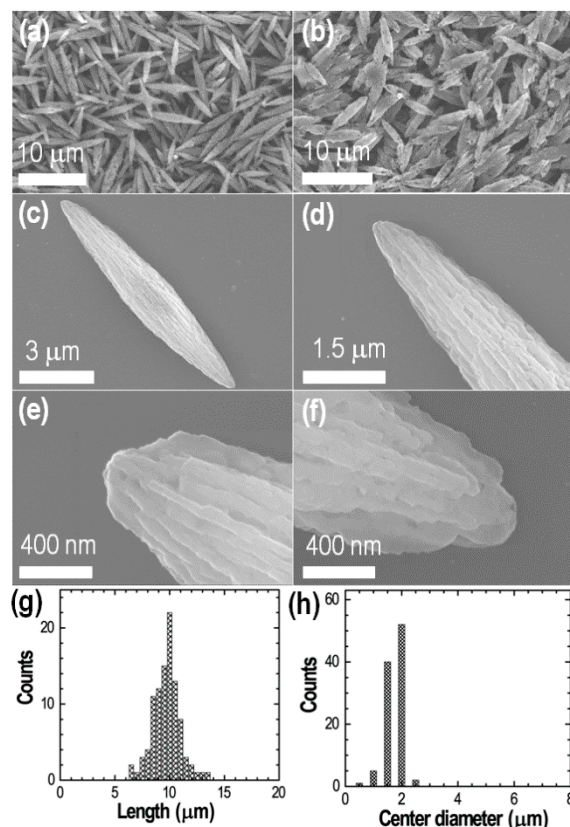


Figure 1. SEM images of fullerene C_{60} crystals self-assembled at a liquid-liquid interface of IPA and C_{60} solution in dodecylbenzene at $25 \text{ }^\circ\text{C}$: (a,b) Low magnification images showing over all surface morphology; (c,d) SEM images of one crystal showing bitter-melon shape; (e,f) High resolution SEM images; (g,h) Histograms of length and diameter distributions.

The crystal structure of the assembled fullerene C_{60} was further characterized by transmission electron microscopy. As revealed by SEM, the bitter melon shape of the crystals is further confirmed by TEM (Figure 2a). Some of the assembled structures are interconnected with crystalline nature as confirmed by the spot-type selected area electron diffraction pattern (inset of Figure 2a). High magnification TEM images revealed the bitter melon shape crystals exhibit nanoporous structures (Figure 2c,d). It is interesting to note that the as-prepared crystals before washing do not have such a nanoporous structure (Figure S3) demonstrating that nanopore formation is caused by the IPA washing. Since fullerene C_{60} is partially soluble in IPA (0.0021 mg/mL), surface dissolution of C_{60} takes place upon washing with IPA. A high resolution TEM (HR-TEM) image shows a dense packed lattice fringes of fullerene with lattice spacing is ca. 0.82 nm corresponding to the distance between two (111) planes of the face-centered cubic (*fcc*) phase of the pristine C_{60} .

The crystal structure of the self-assembled C_{60} is confirmed by powder X-ray diffraction (pXRD) technique. Figure 3 shows diffraction patterns of C_{60} assemblies before and after IPA washing. For comparison, diffraction pattern of pristine C_{60} (pC_{60}) is also included. Bitter melon shaped C_{60} assemblies before IPA washing show intense pXRD peaks at diffraction angles of 10.7° , 17.58° and 20.68° corresponding to (111), (022), and (024), planes of *fcc* crystal phase with the cell dimensions ca. $a = 1.425 \text{ nm}$, and $V = 2.899 \text{ nm}^3$.

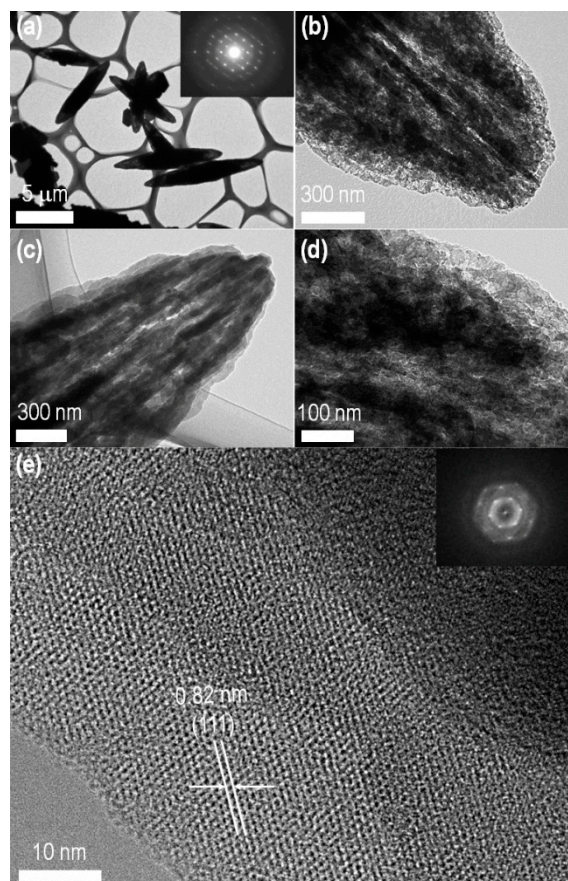


Figure 2. Transmission microscopic images of C_{60} crystals prepared a liquid-liquid interface of IPA and C_{60} solution in dodecylbenzene at 25 °C: (a–d) Low magnification TEM images; (e) HR-TEM image. Insets of panel “a” and “e” represent SAED patterns.

Weak diffraction peaks at diffraction angles of 10.14° and 19° (as highlighted by symbol) corresponds to (101) and (401) planes of *hcp* crystal phase, which is commonly observed in solid solvates due to the entrapment of solvent molecule at the interstitial site of the cubic lattice during crystallization [48,49].

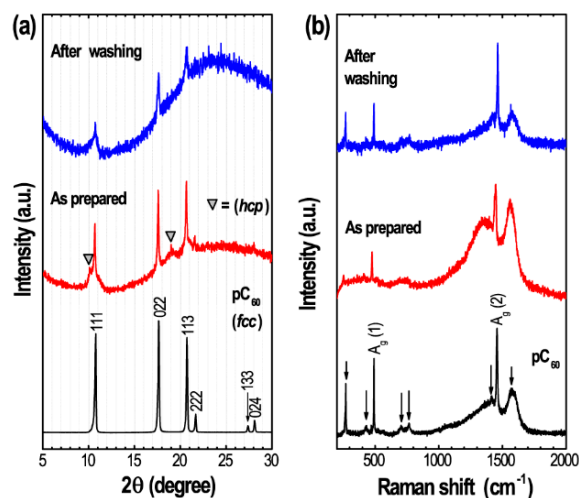


Figure 3. (a) Powder X-ray diffraction (pXRD) of pC_{60} and self-assembled bitter-melon shaped fullerene C_{60} crystals before and after washing; (b) the corresponding Raman scattering spectra recorded at 25 °C.

The diffraction peaks corresponding to *hcp* phase disappear upon washing/and drying of the samples and the samples displays pXRD peaks corresponding to *fcc* phase only with cell dimension ca. $a = 1.427$ nm, and $V = 2.907$ nm³, which are very close to the cell dimension of pristine C₆₀; $a = 1.421$ nm, and $V = 2.871$ nm³. Figure 3b shows Raman scattering spectrum of pC₆₀ and the prepared C₆₀ crystal before and after IPA washing. Raman spectra were recorded upon exciting with a 514.5 nm laser at 25 °C. Raman spectra showed two A_g [A_g(1), and A_g(2)] and six H_g vibration bands [H_g(1), H_g(2), H_g(3), H_g(4), H_g(7) and H_g(8)]. Out of these Raman active bands, the A_g(2) band corresponds to pentagonal pinch mode and has been used as an analytical probe for the structural and optoelectronic properties of fullerene C₆₀ molecule [50]. For instance, a blue shift of A_g(2) band is an indication of polymerization of C₆₀ molecules. The A_g(2) Raman band of bitter melon shaped fullerene C₆₀ crystal remains essentially unchanged before and after washing and is similar to that of pC₆₀. This indicates that molecular C₆₀ dominates in the bitter melon shaped nanoporous fullerene C₆₀ crystal and laser irradiation during measurements did not cause polymerization of C₆₀ molecules, i.e., self-assembled crystals are molecular solid without any chemical bonds between the adjacent C₆₀ molecules.

In order to further confirm the solid solvate structure as revealed by pXRD, we have recorded FT-IR spectra of prepared fullerene C₆₀ crystals before and after washing and compared the data with pC₆₀. Figure 4 shows FT-IR data recorded at 25 °C in low and high wavenumber regions. In addition to four major peaks at 526, 575, 1180 and 1428 cm⁻¹ corresponding to pC₆₀, three additional peaks at 3028, 2924 and 2853.5 cm⁻¹ that corresponds to aromatic (3028 cm⁻¹) and aliphatic (2924 and 2853.5 cm⁻¹) C–H stretching can be seen in the FT-IR spectrum of the as-prepared sample before IPA washing, indicating that the crystals contain some dodecylbenzene solvent molecules, i.e., as prepared crystals are C₆₀ solid solvates. FT-IR bands corresponding to the C–H stretching disappeared and one additional peak at 3445 cm⁻¹ (O–H stretching) appeared the bitter-melon shape crystal after IPA washing.

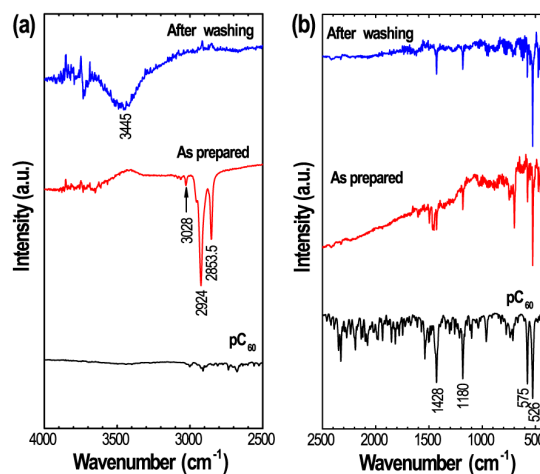


Figure 4. FT-IR spectra of pC₆₀ and self-assembled bitter-melon shaped fullerene C₆₀ crystals before and after washing measured at 25 °C: (a) FT-IR spectra in high wavenumber region; (b) Corresponding FT-IR spectra in low wavenumber region.

Judging from the surface and structural properties, we anticipated that our nanoporous bittermelon shaped fullerene C₆₀ crystals could be suitable candidates for sensing toxic VOCs such as benzene, toluene and aniline, and we have studied the vapor sensing capacities for sensing toxic aromatic solvents using the quartz crystal microbalance (QCM) technique. QCM sensors are favored over other gas analysis techniques such as gas chromatography and mass spectroscopy, as they are compact in size, simple design and provide the real time analysis. Figure 5a shows a typical example of the time dependent frequency shifts (Δf) of the bitter melon shaped nanoporous fullerene C₆₀ crystals modified QCM electrode upon exposure to the different organic solvents vapors; methanol, hexane,

benzene, toluene and aniline. For comparison, frequency shifts upon exposure of water vapors is also included.

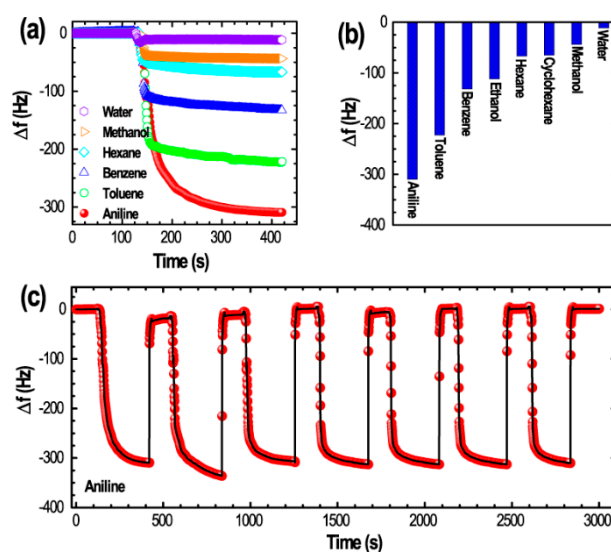


Figure 5. Vapor sensing performance of bitter melon shape nanoporous C_{60} crystals: (a) Frequency shifts (Δf) upon exposure of QCM electrode to water, methanol, hexane, benzene, toluene and aniline as typical example; (b) Summary of sensor performance, and (c) Repeatability test upon exposure and removal of toluene vapors up to seven cycles.

As it can be seen in Figure 5a, the frequency shift is very rapid upon exposure of the QCM sensor to the solvent vapors and when the solvent vapors are removed or air is exposed the frequency goes back to its original position (desorption is also rapid: Figure S4a). Furthermore, the value of frequency shift, which corresponds to the adsorption of gas molecules, strongly depends on the nature of the vapor phase guest molecules. Aromatic solvent vapors caused huge frequency shifts compared to aliphatic hydrocarbons of apparently similar molecular size. Alcohols and water indeed caused only a small change in the frequency (Figure 5b). Frequency shifts caused by the adsorption of aromatic solvent vapors are ca. 310 Hz (aniline), 222 Hz (toluene), 132 Hz (benzene). While the frequency shifts caused by the adsorption of aliphatic solvent vapors are ca. 67 Hz (hexane), 65 Hz (cyclohexane). Frequency shifts caused by the adsorption of ethanol, methanol and water were ca. 111 Hz (ethanol), 43 Hz (methanol) and 11 Hz (water), respectively. QCM results demonstrate that the bitter melon shape nanoporous C_{60} crystals is preferential hosts for aromatic vapors, i.e., they are more selective towards aromatic vapors. The selectivity of QCM sensing decreases in the following order: aniline > toluene > benzene > ethanol > hexane > cyclohexane > methanol > water. We have also tested the repeatability of the QCM electrode upon alternate exposure and removal of aniline vapors (Figure 5c). The electrode showed quite good repeatability without losing sensing performance after seven cycles, demonstrating the potential of the material in QCM device fabrication.

4. Discussion

Environmental pollution has become one of the key problems with the advancement of nanotechnology. Air pollutants, such as VOCs and respirable particulate matter ($PM_{2.5}$ and PM_{10}) diffuse over long or short distances and contaminate the environment. The air polluted with VOCs has both acute and chronic effects on human health, affecting a number of different systems and organs. This ranges from minor upper respiratory tract irritation to chronic respiratory and heart disease, lung cancer, acute respiratory infections, aggravated pre-existing heart and lung diseases, or asthmatic attacks. Both indoor and ambient air is contaminated with toxic VOCs such as toluene, aniline and benzene due to the use of common household products such as paints, adhesives, synthetic

fragrances, and smokes, which are inevitable. Needless to say these VOCs are extremely bad for a healthy environment and life. Therefore, molecular sensing of toxic organic substances has become an important subject and many researchers have been working to design a novel nanomaterials to design functional system to address these environment-related problems [51–54]. Previous investigations have underlined the fact that a well-designed host nanostructure, particularly high surface area nanoporous materials, are essential for enhancing sensor performance [55–60].

Micro/mesoporous hierarchical fullerene nanomaterials are anticipated to display higher efficiency as gas sensors, particularly for aromatic vapors due to their unique π -conjugated structure, high hydrophobicity and strong van der Waals and π - π interactions that contribute greatly to the sensing performance and higher sensing selectivity response to aromatic guests [41,59]. As seen in Figure 5a,b, a higher selectivity towards aromatic solvent vapors compared to the aliphatic hydrocarbon vapors of similar dimensions is caused due to enhanced interaction between sp^2 -featured fullerene assembly with aromatic gases, high-contact probability, and easy diffusions of the guest gases through the mesoporous structure of the bitter-melon-shaped fullerene C_{60} crystals. Since the vapor pressure ($\log(\text{pressure}/\text{mmHg})$) of aromatic solvents benzene (1.978), toluene (1.462) and aniline (0.489) is lower compared to the aliphatic hydrocarbon, *n*-hexane (2.179), the observed higher sensing selectivity towards toluene or pyridine vapors cannot be due to the difference in saturated vapor pressure. It is caused due to a unique structural feature of our material. Sensing performances of as prepared crystals without nanoporous structure and pC_{60} are very poor compared to the nanoporous crystals (Figure S4b) demonstrating the importance of porous structure, which promotes easy diffusion of aromatic solvent vapors into the mesoporous architecture favored by strong π - π interactions between host and guest.

5. Conclusions

We have fabricated self-assembled bitter melon shaped mesoporous C_{60} crystals by a dynamic liquid-liquid interfacial precipitation (LLIP) method at ambient conditions of temperature and pressure. Due to a well-developed mesoporous structure the bitter melon-like fullerene crystals showed excellent vapor sensing performance with higher selectivity towards aromatic vapors. QCM Frequency shifts caused by the adsorption of solvent vapors are ca. 310 Hz (aniline), 222 Hz (toluene), 132 Hz (benzene), 67 Hz (hexane), 65 Hz (cyclohexane), 111 Hz (ethanol), 43 Hz (methanol) and 11 Hz (water) demonstrating that the bitter-melon-shape nanoporous C_{60} crystals are more selective towards aromatic vapors compared to the aliphatic counterparts. The selectivity of QCM sensing decreases in the following order: aniline > toluene > benzene > ethanol > hexane > cyclohexane > methanol > water. We believe that nanoporous fullerene-based nanomaterial would be an asset to the sensing technology, particularly to sense aromatic guest molecules.

Supplementary Materials: The following are available online at <http://www.mdpi.com/1424-8220/19/2/267/s1>, Figure S1: SEM images of as prepared C_{60} crystal before washing: (a–d) Low magnification SEM images showing the aggregated structure; (e,f) High magnification SEM images, Figure S2: Additional SEM images of the crystal after washing showing different shapes, Figure S3: TEM images of as prepared crystal before washing: (a–d) Low magnification TEM images. (e) HR-TEM image. Insets of panel “a” and “e” represent SAED patterns, Figure S4: Additional QCM data: (a) Frequency shifts upon exposure and removal of solvents vapors; (b) Comparison of sensing performance of mesoporous bitter-melon-shape crystals (after washing) with as prepared crystal and pristine C_{60} .

Author Contributions: L.K.S., R.G.S. and Y.Y. conceived and designed the experiments; N.F. and R.G.S. performed the experiments; L.K.S., Y.Y. and T.H. analyzed the data; K.A. contributed reagents/materials/analysis tools. L.K.S., Y.Y. and K.A. discussed the data and wrote the paper.

Funding: This study was partially funded by JSPS KAKENHI Grant Number JP 16H06518 (Coordination Asymmetry) and CREST JST Grant Number JPMJCR1665.

Acknowledgments: Natsumi Furuuchi is thankful to National Institute for Materials Science (NIMS) for NIMS internship award to conduct this study.

Conflicts of Interest: The authors declare no conflict of interest.

References

1. Kroto, H.W.; Heath, J.R.; O'Brien, S.C.; Curl, R.F.; Smalley, R.E. C₆₀: Buckminsterfullerene. *Nature* **1985**, *318*, 162–163. [[CrossRef](#)]
2. Kumar, G.S.; Shrestha, R.G.; Ji, Q.; Hill, J.P.; Ariga, K.; Acharya, S.; Shrestha, L.K. Hierarchical Heterostructure of Ag-Nanoparticle Decorated Fullerene Nanorods (Ag-FNRs) as an Effective Single Particle Freestanding SERS Substrate. *Phys. Chem. Chem. Phys.* **2018**, *20*, 18873–18878. [[CrossRef](#)]
3. Bairi, P.; Shrestha, R.G.; Hill, J.P.; Nishimura, T.; Ariga, K.; Shrestha, L.K. Mesoporous Graphitic Carbon Microtubes Derived from Fullerene C₇₀ Tubes as a High Performance Electrode Material for Advanced Supercapacitors. *J. Mater. Chem. A* **2016**, *4*, 13899–13906. [[CrossRef](#)]
4. Zheng, S.; Ju, H.; Lu, X. A High-Performance Supercapacitor Based on KOH Activated 1D C₇₀ Microstructures. *Adv. Energy Mater.* **2016**, *5*, 1500871. [[CrossRef](#)]
5. Shrestha, R.G.; Shrestha, L.K.; Khan, A.H.; Kumar, G.S.; Acharya, S.; Ariga, K. Demonstration of Ultrarapid Interfacial Formation of 1D Fullerene Nanorods with Photovoltaic Properties. *ACS Appl. Mater. Interfaces* **2014**, *6*, 15597–15603. [[CrossRef](#)]
6. Iijima, S. Helical microtubules of graphitic carbon. *Nature* **1991**, *354*, 56–58. [[CrossRef](#)]
7. Novoselov, K.S.; Geim, A.K.; Morozov, S.V.; Jiang, D.; Zhang, Y.; Dubonos, S.V.; Grigorieva, I.V.; Firsov, A.A. Electric field effect in atomically thin carbon films. *Science* **2004**, *306*, 666–669. [[CrossRef](#)]
8. Rao, A.M.; Zhou, P.; Wang, K.-A.; Hager, G.T.; Holden, J.M.; Wang, Y.; Lee, W.-T.; Bi, X.-X.; Eklund, P.C.; Cornett, D.S.; et al. Photoinduced Polymerization of Solid C₆₀ films. *Science* **1993**, *259*, 955–957. [[CrossRef](#)]
9. Prato, M. [60] Fullerene Chemistry for Materials Science Applications. *J. Mater. Chem.* **1997**, *7*, 1097–1109. [[CrossRef](#)]
10. Ueda, A. Development of Novel Functional Organic Crystals by Utilizing Proton- and π -Electron-Donating/Accepting Abilities. *Bull. Chem. Soc. Jpn.* **2017**, *90*, 1181–1188. [[CrossRef](#)]
11. Sakamoto, R. Bottom-up Creation of Functional Low-Dimensional Materials Based on Metal Complexes. *Bull. Chem. Soc. Jpn.* **2017**, *90*, 272–278. [[CrossRef](#)]
12. Hiroto, S. Innovative Synthesis and Functions of Curved π -Conjugated Molecules. *Bull. Chem. Soc. Jpn.* **2018**, *91*, 829–838. [[CrossRef](#)]
13. Cherumukhil, S.; Vedhanarayanan, B.; Das, G.; Praveen, V.K.; Ajayaghosh, A. Self-Assembly of Bodipy-Derived Extended π -Systems. *Bull. Chem. Soc. Jpn.* **2018**, *91*, 100–120. [[CrossRef](#)]
14. Matsuura, K. Construction of Functional Biomaterials by Biomolecular Self-Assembly. *Bull. Chem. Soc. Jpn.* **2017**, *90*, 873–884. [[CrossRef](#)]
15. Sawada, T.; Serizawa, T. Filamentous Viruses as Building Blocks for Hierarchical Self-Assembly toward Functional Soft Materials. *Bull. Chem. Soc. Jpn.* **2018**, *91*, 455–466. [[CrossRef](#)]
16. Nakamura, E.; Isobe, H. Functionalized Fullerenes in Water. The First 10 Years of Their Chemistry, Biology, and Nanoscience. *Acc. Chem. Res.* **2003**, *36*, 807–815. [[CrossRef](#)]
17. Thompson, B.C.; Fréchet, J.M.J. Polymer-Fullerene Composite Solar Cells. *Angew. Chem. Int. Ed.* **2007**, *47*, 58–77. [[CrossRef](#)]
18. Segura, J.L.; Martín, N.; Guldi, D.M. Materials for Organic Solar Cells: The C₆₀/-conjugated Oligomer Approach. *Chem. Soc. Rev.* **2005**, *34*, 31–47. [[CrossRef](#)]
19. Hoppe, H.; Sariciftci, N.S. Morphology of Polymer/Fullerene Bulk Heterojunction Solar Cells. *J. Mater. Chem.* **2006**, *16*, 45–61. [[CrossRef](#)]
20. Babu, S.S.; Möhwald, H.; Nakanishi, T. Recent Progress in Morphology Control of Supramolecular Fullerene Assemblies and its Applications. *Chem. Soc. Rev.* **2010**, *39*, 4021–4035. [[CrossRef](#)]
21. Liu, H.; Li, Y.; Jiang, L.; Luo, H.; Xiao, S.; Fang, H.; Li, H.; Zhu, D.; Yu, D.; Xu, J.; et al. Imaging As-Grown [60] Fullerene Nanotubes by Template Technique. *J. Am. Chem. Soc.* **2002**, *124*, 13370–13371. [[CrossRef](#)]
22. Tachibana, M.; Kobayashi, K.; Uchida, T.; Kojima, K.; Tanimura, M.; Miyazawa, K. Photo-assisted Growth and Polymerization of C₆₀ Nanowhiskers. *Chem. Phys. Lett.* **2003**, *374*, 279–285. [[CrossRef](#)]
23. Wang, L.; Liu, B.; Liu, D.; Yao, M.; Hou, Y.; Yu, S.; Cui, T.; Li, D.; Zou, G.; Iwasiewicz, A.; et al. Synthesis of Thin, Rectangular C₆₀ Nanorods Using m-Xylene as a Shape Controller. *Adv. Mater.* **2006**, *18*, 1883–1888. [[CrossRef](#)]

24. Geng, J.; Zhou, W.; Skelton, P.; Yue, W.; Kinloch, I.A.; Windle, A.H.; Johnson, B.F.G. Crystal Structure and Growth Mechanism of Unusually Long Fullerene (C₆₀) nanowire. *J. Am. Chem. Soc.* **2008**, *130*, 2527–2534. [[CrossRef](#)]
25. Shin, H.S.; Yoon, S.M.; Tang, Q.; Chon, B.; Joo, T.; Choi, H.C. Highly Selective Synthesis of C₆₀ Disks on Graphite Substrate by a Vapor-Solid Process. *Angew. Chem. Int. Ed.* **2008**, *47*, 693–696. [[CrossRef](#)]
26. Briseno, A.L.; Mannsfeld, S.C.B.; Ling, M.M.; Liu, S.; Tseng, R.J.; Reese, C.; Roberts, M.E.; Yang, Y.; Wudl, F.; Bao, Z. Patterning Organic Single-Crystal Transistor Arrays. *Nature* **2006**, *444*, 913–917. [[CrossRef](#)]
27. Miyazawa, K.; Kuwasaki, Y.; Obayashi, A.; Kuwabara, M. C₆₀ Nanowhiskers Formed by the Liquid-Liquid Interfacial Precipitation Method. *J. Mater. Res.* **2002**, *17*, 83–88. [[CrossRef](#)]
28. Shrestha, L.K.; Ji, Q.; Mori, T.; Miyazawa, K.; Yamauchi, Y.; Hill, J.P.; Ariga, K. Fullerene nanoarchitectonics: From zero to higher dimensions. *Chem. Asian J.* **2013**, *8*, 1662–1679. [[CrossRef](#)]
29. Shrestha, L.K.; Yamauchi, Y.; Hill, J.P.; Miyazawa, K.; Ariga, K. Fullerene crystals with bimodal pore architectures consisting of macropores and mesopores. *J. Am. Chem. Soc.* **2013**, *135*, 586–589. [[CrossRef](#)]
30. Shrestha, L.K.; Shrestha, R.G.; Yamauchi, Y.; Hill, J.P.; Nishimura, T.; Miyazawa, K.; Kawai, T.; Okada, S.; Wakabayashi, K.; Ariga, K. Nanoporous Carbon Tubes from Fullerene Crystals as the π -electron Carbon Source. *Angew. Chem. Int. Ed.* **2015**, *54*, 951–955. [[CrossRef](#)]
31. Sathish, M.; Miyazawa, K.; Hill, J.P.; Ariga, K. Solvent Engineering for Shape-Shifter Pure Fullerene (C₆₀). *J. Am. Chem. Soc.* **2009**, *131*, 6372–6373. [[CrossRef](#)]
32. Miyazawa, K.; Kuwasaki, Y.; Hamamoto, K.; Nagata, S.; Obayashi, A.; Kuwabara, M. Structural Characterization of C₆₀ Nanowhiskers Formed by the Liquid/Liquid Interfacial Precipitation Method. *Surf. Interface Anal.* **2003**, *35*, 117–120. [[CrossRef](#)]
33. Sathish, M.; Miyazawa, K.; Sasaki, T. Nanoporous Fullerene Nanowhiskers. *Chem. Mater.* **2007**, *19*, 2398–2400. [[CrossRef](#)]
34. Masuhara, A.; Tan, Z.; Kasai, H.; Nakanishi, H.; Oikawa, H. Fullerene Fine Crystals with Unique Shapes and Controlled Size. *Jpn. J. Appl. Phys.* **2009**, *48*, 050206. [[CrossRef](#)]
35. Jeong, J.; Kim, W.-S.; Park, S.-I.; Yoon, T.-S.; Chung, B.H. Synthesis and Characterization of Various-Shaped C₆₀ Microcrystals Using Alcohols as Antisolvents. *J. Phys. Chem. C* **2010**, *114*, 12976–12981. [[CrossRef](#)]
36. Shrestha, L.K.; Hill, J.P.; Tsuruoka, T.; Miyazawa, K.; Ariga, K. Surfactant-assisted assembly of fullerene (C₆₀) nanorods and nanotubes formed at liquid-liquid interface. *Langmuir* **2013**, *29*, 7195–7202. [[CrossRef](#)]
37. Shrestha, L.K.; Shrestha, R.G.; Hill, J.P.; Tsuruoka, T.; Ji, Q.; Nishimura, T.; Ariga, K. Surfactant-Triggered Nanoarchitectonics of Fullerene C₆₀ Crystals at a Liquid-Liquid Interface. *Langmuir* **2016**, *32*, 12511–12519. [[CrossRef](#)]
38. Bairi, P.; Tsuruoka, T.; Acharya, S.; Ji, Q.; Hill, J.P.; Ariga, K.; Yamauchi, Y.; Shrestha, L.K. Mesoporous Fullerene C₇₀ Cubes with Highly Crystalline Frameworks and Unusual Enhancement Photoluminescence Properties. *Mater. Horiz.* **2018**, *5*, 285–290. [[CrossRef](#)]
39. Bairi, P.; Minami, K.; Hill, J.P.; Ariga, K.; Shrestha, L.K. Intentional Closing/Opening of “Hole-in-Cube” in Fullerene C₇₀ Crystals with Microscopic Recognition Properties. *ACS Nano* **2017**, *11*, 7790–7796. [[CrossRef](#)]
40. Shrestha, L.K.; Sathish, M.; Hill, J.P.; Miyazawa, K.; Tsuruoka, T.; Sanchez-Ballester, N.; Honma, I.; Ji, Q.; Ariga, K. Alcohol-induced rearrangement of Olmstead’s crystalline Ag(I)-fullerene heteronanostructure yields ‘Bucky Cubes’. *J. Mater. Chem. C* **2013**, *1*, 1174–1181. [[CrossRef](#)]
41. Bairi, P.; Minami, K.; Nakanishi, W.; Hill, J.P.; Ariga, K.; Shrestha, L.K. Hierarchically Structured Fullerene C₇₀ Cube for Sensing Volatile Aromatic Solvent Vapors. *ACS Nano* **2016**, *10*, 6631–6637. [[CrossRef](#)]
42. Oaki, Y. Morphology Design of Crystalline and Polymer Materials from Nanoscopic to Macroscopic Scales. *Bull. Chem. Soc. Jpn.* **2017**, *90*, 776–788. [[CrossRef](#)]
43. Khan, A.H.; Ghosh, S.; Pradhan, B.; Dalui, A.; Shrestha, L.K.; Acharya, S.; Ariga, K. Two-Dimensional (2D) Nanomaterials towards Electrochemical Nanoarchitectonics in Energy-Related Applications. *Bull. Chem. Soc. Jpn.* **2017**, *90*, 627–648. [[CrossRef](#)]
44. Komiyama, M.; Yoshimoto, K.; Sisido, M.; Ariga, K. Chemistry Can Make Strict and Fuzzy Controls for Biosystems: DNA Nanoarchitectonics and Cell-Macromolecular Nanoarchitectonics. *Bull. Chem. Soc. Jpn.* **2017**, *90*, 967–1004. [[CrossRef](#)]
45. Komiyama, M.; Mori, T.; Ariga, K. Molecular Imprinting: Materials Nanoarchitectonics with Molecular Information. *Bull. Chem. Soc. Jpn.* **2018**, *91*, 1075–1111. [[CrossRef](#)]

46. Benzigar, M.R.; Joseph, S.; Baskar, A.V.; Park, D.-H.; Chandra, G.; Umopathy, S.; Talapanei, S.N.; Vinu, A. Ordered Mesoporous C₇₀ with Highly Crystalline Pore Walls for Energy Applications. *Adv. Funct. Mater.* **2018**, *28*, 1803701. [[CrossRef](#)]
47. Benzigar, M.R.; Joseph, S.; Ilbeygi, H.; Park, D.-H.; Sarkar, S.; Chandra, G.; Umopathy, S.; Srinivasan, S.; Talapanei, S.N.; Vinu, A. Highly Crystalline Mesoporous C₆₀ with Ordered Pores: A Class of Nanomaterials for Energy Applications. *Angew. Chem.* **2018**, *130*, 578–582. [[CrossRef](#)]
48. Minato, J.; Miyazawa, K. Solvated Structure of C₆₀ Nanowhiskers. *Carbon* **2005**, *43*, 2837–2841. [[CrossRef](#)]
49. Rana, M.; Bharathanatha, R.R.; Gautam, U.K. Kinetically Stabilized C₆₀-toluene Solvate Nanostructures with a Discrete Absorption Edge Enabling Supramolecular Topotactic Molecular Exchange. *Carbon* **2014**, *74*, 44–53. [[CrossRef](#)]
50. Kuzmany, H.; Matus, M.; Burger, B.; Winter, J. Raman Scattering in C₆₀ Fullerenes and Fullerides. *Adv. Mater.* **1994**, *6*, 731–745. [[CrossRef](#)]
51. Cavallari, M.R.; Braga, G.S.; da Silva, M.F.P.; Izquierdo, J.E.E.; Paterno, L.G.; Dirani, E.A.T.; Kymissis, I.; Fonseca, F.J. A Hybrid Electronic Nose and Tongue for the Detection of Ketones: Improved Sensor Orthogonality Using Graphene Oxide-Based Detectors. *IEEE Sens. J.* **2017**, *17*, 1971–1980. [[CrossRef](#)]
52. Li, X.; Chen, X.; Yu, X.; Chen, X.; Ding, X.; Zhao, X. A High-Sensitive Humidity Sensor Based on Water Soluble Composite Material of Fullerene and Graphene Oxide. *IEEE Sens. J.* **2018**, *18*, 962–966. [[CrossRef](#)]
53. Bahoumina, P.; Hallil, H.; Lachaud, J.-L.; Rebière, D.; Dejous, C.; Abdelghani, A.; Frigui, K.; Bila, S.; Baillargeat, D.; Zhang, Q.; et al. Chemical Sensor Based on a Novel Capacitive Microwave Flexible Transducer with Polymer Nanocomposite-Carbon Nanotube Sensitive Film. *Microsyst. Technol.* **2018**. [[CrossRef](#)]
54. Nasri, A.; Boubaker, A.; Hafsi, B.; Khaldi, W.; Kalboussi, A. Highly-Sensitivity Sensor Using C₆₀-Single Molecule Transistor. *IEEE Sens. J.* **2018**, *18*, 248–254. [[CrossRef](#)]
55. Ding, X.; Chen, X.; Chen, X.; Zhao, X.; Li, N. A QCM Humidity Sensor Based on Fullerene/Graphene Oxide Nanocomposite with High Quality Factor. *Sens. Actuators B Chem.* **2018**, *266*, 534–542. [[CrossRef](#)]
56. Magana, J.R.; Kolen'ko, Y.V.; Deepak, F.L.; Solans, C.; Shrestha, R.G.; Hill, J.P.; Ariga, K.; Shrestha, L.K.; Rodriguez-Abreu, C. From Chromonic Self-Assembly to Hollow Carbon Nanofibers for Efficient Materials in Supercapacitor and Vapor Sensing Applications. *ACS Appl. Mater. Interfaces* **2016**, *8*, 31231–31238. [[CrossRef](#)]
57. Shrestha, L.K.; Adhikari, L.; Shrestha, R.G.; Adhikari, M.P.; Adhikari, R.; Hill, J.P.; Pradhananga, R.R.; Ariga, K. Nanoporous Carbon Materials with Enhanced Supercapacitance Performance and Non-Aromatic Chemical Sensing with C1/C2 Alcohol Discrimination. *Sci. Technol. Adv. Mater.* **2016**, *17*, 483–492. [[CrossRef](#)]
58. Tripathi, K.M.; Kim, T.Y.; Losic, D.; Tung, T.T. Recent Advances in Engineered Graphene and Composite for Detection of Volatile Organic Compounds (VOCs) and Non-Invasive Diseases Diagnosis. *Carbon* **2016**, *110*, 97–129. [[CrossRef](#)]
59. Vimalanathan, K.; Shrestha, R.G.; Zhang, Z.; Zho, J.; Nakayama, T.; Raston, C.L. Surfactant-Free Fabrication of C₆₀ Nanotubules Under Shear. *Angew. Chem. Int. Ed.* **2017**, *56*, 8398–8401. [[CrossRef](#)]
60. Teradal, N.L.; Marx, S.; Morag, A.; Jelinek, R. Porous Graphene Oxide Chemi-Capacitor Vapor Sensor Array. *J. Mater. Chem. C.* **2017**, *5*, 1128–1135. [[CrossRef](#)]

